



# University of HUDDERSFIELD

## University of Huddersfield Repository

Kollar, László E. and Farzaneh, Masoud

Wind-tunnel investigation of icing of an inclined cylinder

### Original Citation

Kollar, László E. and Farzaneh, Masoud (2010) Wind-tunnel investigation of icing of an inclined cylinder. *International Journal of Heat and Mass Transfer*, 53 (5-6). pp. 849-861. ISSN 0017-9310

This version is available at <http://eprints.hud.ac.uk/16078/>

The University Repository is a digital collection of the research output of the University, available on Open Access. Copyright and Moral Rights for the items on this site are retained by the individual author and/or other copyright owners. Users may access full items free of charge; copies of full text items generally can be reproduced, displayed or performed and given to third parties in any format or medium for personal research or study, educational or not-for-profit purposes without prior permission or charge, provided:

- The authors, title and full bibliographic details is credited in any copy;
- A hyperlink and/or URL is included for the original metadata page; and
- The content is not changed in any way.

For more information, including our policy and submission procedure, please contact the Repository Team at: [E.mailbox@hud.ac.uk](mailto:E.mailbox@hud.ac.uk).

<http://eprints.hud.ac.uk/>

## Wind-Tunnel Investigation of Icing of an Inclined Cylinder

László E. Kollár\* and Masoud Farzaneh

NSERC/Hydro-Québec/UQAC Industrial Chair on Atmospheric Icing of Power Network  
Equipment (CIGELE) and Canada Research Chair on Engineering of Power Network

Atmospheric Icing (INGIVRE) [www.cigele.ca](http://www.cigele.ca)

Université du Québec à Chicoutimi, 555 boulevard de l'Université, Chicoutimi, Québec,  
Canada, G7H 2B1

### Abstract

The effects of varying the angle of wind velocity and axis of a cylindrical icing object around all of the three mutually perpendicular axes are studied experimentally. The mass, shape and profile of ice accretion obtained in a horizontal icing wind tunnel are investigated as functions of cylinder inclination. The icing object is exposed to two types of aerosol cloud, which are created by different procedures: (i) injecting small droplets horizontally into cold air flow, (ii) injecting vertically falling large droplets into cold air flow; so that the resulting conditions simulate in-cloud icing and freezing rain, respectively. Observations reveal the effects of varying each angle on the mass, shape and profile of ice accreted under both conditions.

*Keywords:* atmospheric icing, inclined cylinder, supercooled water film, wind-tunnel experiments

### Nomenclature

$l$  unit length of cylinder

$m$  ice mass

$m_{CI,\alpha_0}$  ice mass obtained under in-cloud icing (CI) conditions with increased liquid water content (LWC) for  $\alpha = 0^\circ$

---

\* Corresponding author, Tel.: +1 (418) 545-5011 / 5606, Fax: +1 (418) 545-5012, E-mail:  
[laszlo\\_kollar@uqac.ca](mailto:laszlo_kollar@uqac.ca)  
URL: <http://www.cigele.ca>

$m_{CIup,\beta_0}$	ice mass obtained under CI conditions with increased LWC upstream of cylinder midpoint for $\beta = 0^\circ$
$m_{ZR,\alpha_0}$	ice mass obtained under freezing rain (ZR) conditions for $\alpha = 0^\circ$
$m_{ZR,\beta_0}$	ice mass obtained under ZR conditions for $\beta = 0^\circ$
$m_{ZRup,\gamma_0}$	ice mass obtained under ZR conditions upstream of cylinder midpoint for $\gamma = 90^\circ$
$t$	time
$T_{a,SB}$	air temperature in tunnel section preceding spray bar
$T_{a,TS}$	air temperature in test section
$V_a$	air velocity in test section
<i>Greek symbols</i>	
$\alpha$	angle of cylinder around streamwise axis in vertical plane
$\beta$	angle of cylinder around vertical axis in horizontal plane
$\gamma$	angle of cylinder around lateral axis in vertical plane
$\Delta$	fluctuation

## 1 Introduction

Most of the atmospheric icing models consider a cylindrical icing object placed in an air flow carrying a supercooled droplet cloud so that the cylinder axis is perpendicular to air velocity. Such a geometrical arrangement involves the possibility to simplify the mathematical model to a two-dimensional (2D) representation. This simplification is advantageous when the droplets of the aerosol cloud freeze immediately upon impact as is the case under extremely cold conditions. However, when the ambient conditions are favorable to the appearance of supercooled water on the surface of the accreting ice, or especially, when the axis of the icing object forms an angle with the air velocity, then the need of 3D models arises for reliable simulation. Scallop formations, which are observed on swept wings in aircraft icing when the sweep angle is high enough [1], are also 3D structures. Surveys and collections of literature on modeling atmospheric ice accretion on

power network equipments are found in [2] and in [3]. A review on modeling ice accretion on swept wings is presented in [4].

The cylindrical icing object may be inclined in three directions relatively to the air flow as sketched in Fig. 1: (i) the cylinder is oriented perpendicularly to air velocity (position at  $0^\circ$ ) and forms an angle,  $\alpha$ , around the streamwise axis in the vertical plane; (ii) the cylinder is oriented perpendicularly to air velocity (position at  $0^\circ$ ), and then its angle,  $\beta$ , is varied around the vertical axis in the horizontal plane; (iii) the cylinder is oriented parallel to air velocity (position at  $90^\circ$ ), and then its angle,  $\gamma$ , is varied around the lateral axis in the vertical plane. The main goal of the present research is to investigate experimentally the effects of the three angles defined on the characteristics of the ice accreted on cylindrical icing bodies. In order to achieve this goal, a cylinder was placed in the test section of a horizontal icing wind tunnel where the aerosol cloud is created by injecting water droplets into the circulating cold air flow. A subsidiary goal is to study whether the influence of cylinder inclination is dissimilar under different icing conditions modeled by aerosol clouds with different droplet size distributions as well as with different manners of water supply. In particular, two atmospheric icing phenomena are simulated: (i) in-cloud icing (CI) and (ii) freezing rain (ZR). The diameter of ordinary cloud droplets falls in the range of 1-2  $\mu\text{m}$  to 40-50  $\mu\text{m}$  [5-7]; thus, the movement of these droplets is not affected to a great extent by gravity, and the aerosol cloud may be modeled by injecting small droplets horizontally into the cold air flow. The range of droplet size in freezing drizzle (ZL) and ZR covers diameters from 50 to 500  $\mu\text{m}$ , and from 500  $\mu\text{m}$  to 3-4 mm, respectively [6]; therefore the effect of gravity on droplet trajectories is significant, and the phenomenon may be simulated by injecting vertically falling large droplets atomized from precooled water into the cold air flow. A series of experiments were carried out in a preceding study [8], which was completed recently by further sets of experiments. The complete study, which was thus implemented in two steps, forms the subject of the present paper.

## **2 Experimental Setup**

### **2.1 Facilities**

The experiments were carried out in the CIGELE atmospheric icing research wind tunnel, a horizontal closed-loop low-speed wind tunnel, 30 m in total length, including a 3 m long test section with a rectangular cross-section, 0.46 m high and 0.92 m wide (see Fig. 2). The temperature in the test section may be cooled down to  $-25^{\circ}\text{C}$ . The velocity of circulating air in the test section may reach a maximum of 30 m/s. The icing object, a cylinder of 0.92 m in length and 0.038 m in diameter, was fixed in the middle of test section, and its inclination was changed with the help of special devices. To vary the angle,  $\alpha$ , of the cylinder around the streamwise axis, the endpoints of the cylinder were fixed to two adjustable supports on the tunnel wall. The length of the supports was varied to achieve the required angle. To vary the angle,  $\beta$ , around the vertical axis, the cylinder was fixed in a support which may be rotated around the vertical axis passing through the midpoint of the support. To vary the angle,  $\gamma$ , around the lateral axis, one edge of the cylinder was hung to the tunnel ceiling, while the other one was supported from the bottom with different support lengths for obtaining different angles. In all cases, special care was taken in order to keep the midpoint of the cylinder at the tunnel centreline. The cylinder was rotated in one direction only around the streamwise and vertical axes, since the droplet cloud is symmetric in the central part of the cross section at the middle of the test section where the ice samples were taken from. The reader is referred to [9] for a more detailed discussion on the zone of uniformity. However, the inclination of the cylinder was varied in both directions around the lateral axis. The limits of the angles which could be achieved were determined by the geometry of the set-up.

Two means of water supply were applied to model different icing conditions. The first one included a horizontal spray bar with three air-assisted nozzles located at the midpoint of the tunnel cross-section, with 20 cm at left and right of this location (Fig. 3). The nozzles are manufactured by Spraying Systems Co., and consist of a 2050 stainless steel water cap and 67147 stainless steel air cap. This system can create an aerosol cloud with a median volume diameter (MVD) of 25 to 70  $\mu\text{m}$ , which models CI. The LWC of the produced cloud may be varied from 0.3 to 12  $\text{g}/\text{m}^3$ . Water at room temperature was used for atomization, although the temperature of injected water droplets was significantly lower due to the cooling effect of cold air which circulated in the tunnel and surrounded the spray bar. The

spray bar with the nozzles was located 4.4 m upstream from the icing cylinder, which distance is sufficient for droplets to become supercooled. This distance is also long enough for water droplets to be mixed in the air flow and to obtain a uniform aerosol cloud in the middle of the test section where the icing object is placed. The other way for supplying water meant the application of a single nozzle mounted on an aluminum rake which was attached to the ceiling of the test section and which was movable horizontally (Fig. 4). The distance was set at 0.4 m upstream from the icing cylinder in these experiments. This setup included a type H ¼ VV – 11005 VeeJet brass nozzle, also from Spraying Systems Co. The nozzle produced an aerosol cloud with ellipsoidal cross section. This nozzle was always used with the same water flow rate for creating an aerosol cloud which models ZR conditions. Since the distance between the nozzle and the icing object is not sufficient for significant cooling of droplets of this size, the water was cooled down to around 4 °C by a commercially designed machine manufactured by CIMCO. The water was further cooled in the water pipe leading to the nozzle, because the pipe passes through the cold test section. The temperature of the water at injection was measured by an Omega T type thermocouple at a distance of 2.54 cm from the nozzle edge inside the water line, and it was usually found to be between 1 °C and 2 °C.

## **2.2. Selecting Experimental Conditions**

Investigating the effects of air temperature and air velocity in detail was out of the scope of this study; consequently, they were kept constant in most of the experiments at values corresponding to what occur during both CI and ZR. The air temperature was set at  $-10 \pm 0.8$  °C in the tunnel section preceding the spray bar, which resulted in an air temperature of  $-8.7 \pm 1.0$  °C in the test section. The air temperature at ground level during ZR is usually above that range, but the lowest observed temperature reaches these values [6]. Also, the relatively short distance between the nozzle and the icing object does not ensure the cooling of droplets down to the same temperature as observed in nature under the same ambient temperature. Further values of air temperature set in the experiments are presented in Table 1 together with their fluctuation. When the desired air temperature was colder, the

difference between the air temperatures in the tunnel section preceding the spray bar and in the test section was greater, because the test chamber only got moderately cool, thus causing the test section temperature to rise. On the other hand, the colder the air temperature was the more its fluctuation diminished. The air velocity in most of the experiments was set at  $20 \text{ m/s} \pm 1\%$  in the test section, although some experiments were also carried out with different air velocities as presented in Section 3.1.3. The air velocity dropped by  $4 - 8\%$  at the end of each experiment depending on the LWC, which drop resulted from ice accumulation on the fan blades and on the vanes located in the corners of the tunnel. The liquid water content (LWC) of the aerosol cloud modeling CI was set at  $1 \text{ g/m}^3$ , but a further series of experiments was carried out with a LWC of  $3.2 \text{ g/m}^3$ , with the other parameters unchanged. Although this latter value is significantly higher than that characterizing CI conditions, it was used to study the effect of LWC, which accelerated the experiments, because a higher amount of ice kept accreting in a shorter time on the icing body. The higher value of LWC also made it possible to study how the angles varied influence pendant ice formation. The LWC and droplet size were controlled by the nozzle-dynamic parameters, i.e. the pressure in the channels supplying water and air to the nozzles. A formula describing the relationship between the LWC and the nozzle-dynamic parameters was proposed in [9] with an estimated maximum discrepancy of  $\pm 20\%$ . The error in the measured MVD was evaluated in [10] at  $\pm 4.5 \mu\text{m} \pm 5\%$ . The pressure in the channels supplying water and air to the air-assisted nozzles were adjusted to  $193 \text{ kPa}$  and  $276 \text{ kPa}$ , respectively, for producing a droplet cloud with MVD of  $35 \mu\text{m}$  and with LWC of  $1 \text{ g/m}^3$ . These pressures were chosen at  $235 \text{ kPa}$  and  $276 \text{ kPa}$  in order to increase the LWC of the cloud to  $3.2 \text{ g/m}^3$ , without changing MVD significantly, which was increased to  $40 \mu\text{m}$  this way. When simulating ZR conditions the flow rate of water supplying the VeeJet brass nozzle was measured during the experiments, and was kept constant at  $0.9 \text{ l/min}$  in order to produce a droplet cloud with MVD of  $800 \mu\text{m}$  and with LWC of  $2.8 \text{ g/m}^3$ . The duration of each experiment was 15 minutes.

### **2.3 Procedure for Collecting Experimental Data**

The following data were collected after each experimental trial: mass of ice accretion per unit length of cylinder, ice shape, and profile of ice accretion. Ice shapes were recorded by taking photos of their front, top and bottom views. In order to measure ice mass, the cylinder was carefully taken off its supports and set into the specially designed support for further examination outside the tunnel. A thin preheated aluminum cutter was used to cut the ice specimens for measuring their mass and length. Samples with length of about 10 cm were taken from the middle of the cylinder, or from the two sides of the midpoint of the cylinder. The maximum error in the measured mass per unit length owing to the fluctuation in the experimental conditions and to the precision of the measurement process was evaluated at  $\pm 10\%$ . After cutting the ice accretion, additional photos were taken to record ice profiles.

### **3 Results and Discussion**

This section discusses the effect of varying the three angles on the mass, shape and profile of ice accretion for CI conditions with normal and with increased LWC, and for ZR conditions.

#### **3.1 Icing of Cylinder Inclined in Vertical Plane around Streamwise Axis**

##### *3.1.1 Ice Profile and Shape*

The maximum angle of the cylinder placed perpendicularly to the flow with the horizontal plane,  $\alpha$ , was limited to  $28^\circ$  by geometrical constraints. The profile of ice accretion under CI conditions does not change so visibly as under CI conditions with increased LWC or under ZR conditions. Therefore, only the first photo in Fig. 7 shows the profile as obtained for  $4^\circ$  under CI conditions, but two series of six photos as obtained for six different angles are presented in Figs. 5 and 6 for the other two conditions. The corresponding two sets of experiments were carried out in a preceding study [8]. However, the ice mass measured in that study for different values of angle,  $\alpha$ , under ZR conditions seemed to be affected by measurement errors so that it was difficult to recognize a tendency; therefore this set of experiment was repeated recently. According to Fig. 5, the ice deposit obtained under CI conditions with increased LWC turns up and becomes narrower, while the pendant



formation at the bottom of the cylinder becomes thicker and more integrated into the entire deposit when the angle,  $\alpha$ , increases. Simultaneously, the limits of impingement decrease. When ZR conditions are modeled, ice accretes around the whole circumference as may be observed in Fig. 6. This fact is mainly ascribed to the sort of water supply and to its location relative to the icing body. Further significant differences are that the stagnation line is not visible and that the plateau of smooth ice surface around the stagnation line does not fall in the vertical plane, but turns up correspondingly to the trajectory of the droplets colliding with the icing object. The pendant formation on the bottom of the accretion forms an angle with the vertical direction. This angle decreases and the pendant formation becomes more indivisible from the entire deposit with an increase of the angle of cylinder inclination. Fig. 7 compares the profile, the top, front, and bottom views of ice accretions obtained for the same angle under the three conditions modeled. This series of photos clearly shows the effect of LWC. When the LWC is lower, the ice deposit is tightly packed, whereas pendant ice forms for higher values of LWC.

### 3.1.2 Ice Mass

The accretion mass per unit length shows an interesting dependence on cylinder angle,  $\alpha$ , around the streamwise axis. Fig. 8a presents mass per unit length,  $m/l$ , under CI conditions with normal and with increased LWC divided by the mass per unit length obtained for  $0^\circ$  under CI conditions with increased LWC,  $m_{CI,\alpha_0}/l$ . Maxima of ice growth mass appear at angle values between  $8-10^\circ$  for both conditions. This finding may be explained by the mass transfer of supercooled water on the cylinder surface. When the angle,  $\alpha$ , increases, a droplet takes a longer time to reach the bottom of the cylinder; thus, the probability of the droplet freezing before shedding increases. However, if the angle,  $\alpha$ , is great enough then the droplet flows faster on the surface due to gravity, so that the probability of droplet freezing before shedding decreases. This tendency was also provided by the morphogenetic model of [11]. The angle of inclination was changed by an increment of  $5^\circ$  in that study, and a maximum was obtained for an inclination angle of  $5^\circ$ . Since the amount of unfrozen water flowing on the surface decreases with decreasing LWC, the variation of ice mass with angle,  $\alpha$ , diminishes significantly for lower values of LWC. In case of CI conditions

with increased LWC, two ice samples from the upper and lower parts of the cylinder near its midpoint were weighed for some angles, and that maximum was observed for both locations. Maxima appear for approximately the same angle; however, their values are different, the maximum ice masses are 12% and 20% greater on the upper and on the lower part of the cylinder, respectively, than the accreted mass measured at  $0^\circ$ . Moreover, the mass of accreted ice on the lower part is always a few percent greater than that on the upper part. Fig. 8a also suggests that the mass of accreted ice is linearly proportional to the LWC, because the ice mass is 3.1 – 3.5 times greater when the LWC is increased by a factor of 3.2. This result is in agreement with the fact that the rate of icing on a unit area of the icing object is determined by the LWC, velocity, collection efficiency, sticking efficiency and accretion efficiency of the impinging particles (see e.g. [2]). LWC is the only parameter which changes significantly in this comparison. The only exception occurs for the highest angle considered; however, the measured value at  $25^\circ$  with the lower LWC seems to be out of tendency for some reason.

The mass of accreted ice shows a similar dependence on cylinder angle,  $\alpha$ , under ZR conditions; however, the mass varies with the angle to a lower extent as under CI conditions with increased LWC, and the maximum is not so striking either. Fig. 8b presents mass per unit length,  $m/l$ , under ZR conditions divided by the mass per unit length obtained at  $0^\circ$  under the same conditions,  $m_{ZR,\alpha_0}/l$ . A further coincidence with the results obtained for CI conditions is that the ice mass on the lower part of the cylinder is slightly greater than on the upper part in most of the measurements. Fig. 8b also shows the ice mass obtained at  $0^\circ$  under CI conditions, which helps conclude that the ice mass under ZR conditions is in the same range, or slightly higher than that under CI conditions with increased LWC. In these cases, the difference in LWC is less than 15%. The collection efficiency is significantly greater for ZR conditions, because droplets are an order of magnitude greater. However, the sticking and accretion efficiencies are smaller, because the distance between the nozzle and cylinder is less in this case; thus, there is not enough time for the larger droplets to get supercooled, and more impinging droplets shed, which slows down the accumulation process.

### *3.1.3 Effect of Thermodynamic Parameters*

The influence of the angle,  $\alpha$ , is compared to the influence of other thermodynamic parameters, air temperature and air velocity, by carrying out additional experiments under CI conditions with increased LWC and with modified thermodynamic parameters at  $\alpha = 0^\circ$ . The modified values of air temperature in the tunnel section preceding the spray bar were  $-20^\circ\text{C}$ ,  $-15^\circ\text{C}$  and  $-5^\circ\text{C}$ , whereas the air velocity in the test section was set at 10 m/s and 30 m/s at the beginning of these tests. The experimental results presented in Fig. 9 prove that, although the effect of angle,  $\alpha$ , is not negligible, changes in the thermodynamic parameters influence the mass of accreted ice to a greater extent than the angle. It may also be concluded from Fig. 9 that the mass of ice accretion increases with air velocity in the range considered, although this result is affected by the vertical separation of droplets of different size [9]. When the velocity is low (10 m/s), the trajectories of big droplets are deflected so that they do not contribute significantly to the ice accumulation on the cylinder placed at mid-height in the test section. The deflection of droplet trajectories becomes small when the air velocity reaches 20 m/s, so that the accreted mass increases considerably. However, a further increase in the air velocity does not cause a comparable change in the mass of ice accretion. The increasing effect of air velocity was also predicted by the model proposed in [12] and observed experimentally in [13]. Although the authors worked with higher velocities (30 – 120 m/s), they reported an increase of ice accretion with air velocity up to about 60 m/s. Concerning air temperature, when it varies between  $-17.5^\circ\text{C}$  and  $-4.5^\circ\text{C}$ , the accreted mass reaches a maximum in the experiments with  $-8.7^\circ\text{C}$ . A maximum at  $-10^\circ\text{C}$  was similarly predicted by the morphogenetic model of [11]. LWC also has a great influence on both the mass and the shape of ice accretion, as was discussed in Sections 3.1.1 and 3.1.2.

### *3.1.4 Evolution of Ice Accretion in Time*

Fig. 10 shows the time evolution of the shape of ice deposit obtained for angles of  $\alpha = 4^\circ$  and  $\alpha = 28^\circ$  under CI conditions with increased LWC [8]. That figure reveals that a major reason for the variation of ice mass with the angle,  $\alpha$ , is the redistribution of supercooled unfrozen water on the cylinder surface and, later, on the ice surface from the raised to the

lowered edge due to gravity. For  $\alpha = 4^\circ$ , supercooled water is moved to the bottom of the cylinder by the combined effect of gravity and air shear force. For  $\alpha = 28^\circ$ , however, gravity overcomes the air shear force and compels the water film to flow mainly lengthwise on the cylinder. Consequently, the pendant ice formation begins earlier for lower values of angle,  $\alpha$ . The first pair of pictures ( $t = 4$  min) does not show pendant ice which appears after  $t = 5$  min of accumulation for  $\alpha = 4^\circ$  and after  $t = 9$  min of accumulation for  $\alpha = 28^\circ$  (compare the second and third pairs of pictures in Fig. 10). The pendant ice formation is already in a developed phase after  $t = 14$  min for both angles; but the shape of ice deposit is still considerably different resulting from the dissimilar mass transfer processes already explained.

### **3.2 Icing of Cylinder Inclined in Horizontal Plane around Vertical Axis**

#### *3.2.1 Ice Profile and Shape*

The rotation of cylinder in the horizontal plane around the vertical axis was not limited by geometrical constraints; therefore, experiments were carried out with angle,  $\beta$ , up to  $70^\circ$ . Similarly to the case of angle,  $\alpha$ , described in Section 3.1, the changes in ice-accretion profiles obtained for different angles,  $\beta$ , under CI conditions are more distinguishable for higher values of LWC. Fig. 11 shows a sequence of pictures about these profiles up to  $\beta = 50^\circ$ . Pendant ice forms up to  $30^\circ$ , then the ice deposit becomes more and more tightly packed, a flat plateau occurs at the stagnation line, and the limits of impingement decrease as the angle,  $\beta$ , increases. This latter observation is mainly explained by the change of droplet trajectories with inclination of the icing object [14]. The air velocity component normal to the cylinder axis decreases with the angle,  $\beta$ , and, consequently, so does the inertia. Thus, the flow deflects droplet trajectories more easily resulting in lower collection efficiency and reduced limits of impingement.

The pictures in Fig. 12 compare the top views of ice deposits obtained for four different values of the angle,  $\beta$ , under the three conditions considered. This set of pictures reveals how scallop formation depends on the angle,  $\beta$ , and on the ambient conditions. When modeling CI conditions, scallops form at angles of minimum  $20^\circ - 25^\circ$ , and complete

scallop occur at angles  $\beta \geq 30^\circ$ . When LWC increases, scallops are incomplete for  $\beta = 30^\circ$ , and complete scallops form at angles around  $40^\circ$  and higher. Complete scallop formation is not distinguishable under ZR conditions. Consequently, scallop formation appears for lower angles when LWC is lower and other parameters are unchanged. This finding coincides with the observation of [1]. Although ice accretion was studied on a swept wing tip, the variation of sweep angle in their case has similar effects as that of the variation of angle,  $\beta$ , in case of an icing cylinder. They observed complete scallop formation for higher angles than the ones presented here, but they worked with significantly higher air velocities which were in the range of 33 m/s (75 mph) to 89 m/s (200 mph), and they also reported that the minimum angle at which complete scallops formed decreased with air velocity.

### 3.2.2 Ice Mass

Fig. 13 shows the effect of angle,  $\beta$ , on the mass of ice accretion. The ice mass decreases with the angle,  $\beta$ , under CI conditions. When the LWC is higher, this decrease is slower for small angles ( $\beta < 30^\circ$ ), while it is faster for large angles ( $\beta > 30^\circ$ ). Also in this case, two ice samples upstream and downstream of the midpoint of the cylinder were taken, and it was found that the weigh of the upstream sample was always a few percent higher than that of the downstream one. Since the cylinder rotates in the horizontal plane when modifying the angle,  $\beta$ , supercooled water does not flow lengthwise on the cylinder due to gravity. Thus, the decrease in ice mass per unit length with increasing angle,  $\beta$ , is mostly a consequence of the decreasing water flow across a unit cylinder surface.

The dependence of ice mass on angle,  $\beta$ , appears to be significantly different under ZR conditions, as may be observed in Fig. 13b. The ice mass does not decrease with increasing angle. On the contrary, it slightly increases for small angles (up to  $30^\circ$ ), and then remains approximately constant. This different behavior may principally be explained by the flow direction of the aerosol cloud. The trajectory and velocity of colliding droplets have both horizontal and vertical components when modeling ZR. Therefore, the water flow across a unit cylinder surface does not decrease to a great extent when the angle,  $\beta$ , approaches  $90^\circ$ , as it happens when the cylinder is exposed to an aerosol cloud moving horizontally. The

masses obtained for  $0^\circ$  under CI conditions are also indicated in Fig. 13b. The masses of accreted ice occur in the same range under ZR conditions and under CI conditions with increased LWC for  $0^\circ$ , although they diverge under these two conditions as the angle,  $\beta$ , increases, due to the different tendencies mentioned above.

### **3.3 Icing of Cylinder Inclined in Vertical Plane around Lateral Axis**

#### *3.3.1 Ice Profile and Shape*

The angle,  $\gamma$ , of cylinder placed in the vertical plane which is parallel to the flow was changed between  $61^\circ$  and  $90^\circ$  in both directions around the lateral axis. The limiting values were determined by geometrical constraints. The negative angle corresponds to the case when the top half of the cylinder is exposed to the air flow, whereas the positive angle corresponds to the case when the bottom half of the cylinder is exposed. Only the sets of experiments under CI conditions with increased LWC and under ZR conditions were carried out with different values of angle,  $\gamma$ , in a preceding study [8], because the variation of ice shape and mass is better observable for higher values of LWC as was concluded in Sections 3.1 and 3.2. The side views of ice deposits formed for different angles,  $\gamma$ , under CI conditions with increased LWC are shown in Fig. 14. The pictures are organized to facilitate comparison of ice deposits obtained for approximately the same angles with opposite signs. Ice accretions for the same absolute values of angle,  $\gamma$ , seem similar; however, the influence of gravity on ice shape and mass may be noticed in a better way on the accretions obtained under ZR conditions (see Figs. 15 and 16). Gravity impedes supercooled water flow on the surface of cylinder or ice due to air shear stress for negative values of angle,  $\gamma$ , while it magnifies the effect of air shear stress for positive values of that angle. It should be noted that when varying the angle,  $\beta$ , this asymmetry in the effects of gravity and air shear force, and consequently, in the ice shape does not appear. Scallop formation can clearly be seen for all the considered values of angle,  $\gamma$ , which is not surprising, because all of these angles are greater than  $60^\circ$  in absolute value, and scallops form for those angles even for the higher value of LWC as was observed in Section 3.2.1. A further observation from Fig. 14 is that the limits of impingement decrease with increasing

absolute value of angle,  $\gamma$ . However, the amount of frozen droplets spread on the bare part of the cylinder increases, which is a consequence of the flow geometry.

Fig. 15 presents a series of pictures on the profiles and on the top or side views of ice deposits obtained under ZR conditions for different values of angle,  $\gamma$ . Similarly to the observation made in Section 3.1.1, ice accretes around the whole circumference of the cylinder when the type of water supply modeling ZR is applied. The shapes of accretions obtained for similar absolute values of angle,  $\gamma$ , are different, and these differences are more visible than those in Fig. 14 for CI conditions with increased LWC. A reason for this asymmetry is the amplifying and opposing effects of gravity and air shear force on droplet movement for positive and negative values of the angle,  $\gamma$ , respectively. This asymmetry is further magnified when modeling ZR conditions due to the vertical component in the trajectory of colliding droplets. Scallop formation may be observed for all the angles considered, although scallops are not as distinguishable as under CI conditions with increased LWC, which results from the different flow geometry.

### 3.3.2 Ice Mass

The mass of ice accreted on a unit length of the cylinder,  $m/l$ , for different values of angle,  $\gamma$  is divided by the ice mass per unit length obtained upstream of the midpoint of the horizontally placed cylinder ( $\gamma = 90^\circ$ ) under ZR conditions,  $m_{ZRup,\gamma_0} / l$ , in order to facilitate the comparison of results measured under different ambient conditions. Fig. 16 plots the resulting values for CI conditions with increased LWC and for ZR conditions upstream and downstream of the midpoint of the cylinder. It is clearly seen in this figure that a minimum of ice mass occurs at  $\gamma = 90^\circ$ , although experiments with  $\gamma = 90^\circ$  were not reliable due to the influence of the cylinder support. This experiment was not even carried out when a horizontally moving aerosol cloud was produced to model CI conditions with increased LWC. On the other hand, the mass per unit length shows similar dependences on the angles,  $\beta$  and  $\gamma$ , in the overlap region ( $60^\circ - 70^\circ$ ). Its rates of decrease with increasing angles are similar under CI conditions with increased LWC, while it is approximately constant under ZR conditions. Contrarily to the cases of angles,  $\alpha$  and  $\beta$ , there is no symmetry around  $\gamma = 0^\circ$ . The mass decreases with angle,  $\gamma$ , more rapidly so when the

bottom half of the cylinder is exposed to the flow, and this asymmetry is more significant under ZR conditions. The reasons for this asymmetry are mentioned in Section 3.3.1.

The comparison of the effects of other thermodynamic parameters and angles,  $\beta$  and  $\gamma$  is not discussed in detail. Since the water flow per unit cylinder surface is reduced drastically when the cylinder is placed closely parallel with the flow ( $\beta$  or  $\gamma$  approaches  $90^\circ$ ), the mass of ice accretion changes more significantly with these angles than with angle,  $\alpha$ , and the changes due to the variation of these angles and due to air velocity or air temperature are comparable.

#### **4 Concluding Remarks**

The dependence of the mass and shape of ice deposits accreted on an inclined cylinder on the angles around the three mutually perpendicular axes was investigated in an icing wind tunnel. Two different water supplies were applied to model three different icing conditions: CI conditions with normal and with increased LWC, and ZR conditions. The main observations regarding the effects of the three angles as they are varied may be summarized as follows:

- The ice mass accreted on a unit length of a cylinder rotated in the vertical plane around the streamwise axis reaches a maximum for an angle,  $\alpha$ , which is approximately  $8^\circ - 10^\circ$  for all the icing conditions examined.
- The ice mass accreted on a unit length of a cylinder rotated in the horizontal plane around the vertical axis decreases monotonically as the angle,  $\beta$ , increases when the cylinder is exposed to an aerosol cloud moving horizontally in order to simulate CI. However, when the velocity of the aerosol cloud has both horizontal and vertical components as in the simulations of ZR, the ice mass per unit length increases slightly for small angles, and then it becomes approximately constant. The range of increasing, decreasing and constant tendencies is expected to depend greatly on the flow direction of the aerosol cloud.
- The ice mass accreted on a unit length of a cylinder rotated in the vertical plane around the lateral axis decreases with the angle of rotation,  $\gamma$ , in the domain



considered. The results obtained for the same values of the angles,  $\beta$  and  $\gamma$ , suggest that the dependences on the two angles are qualitatively similar. However, unlike for the angles of rotation around the other two axes, the dependences are not identical for positive and negative values of the angle,  $\gamma$ . The decreasing tendency is faster when the bottom half of the cylinder is exposed to the flow.

Experiments with different values of LWC show that the mass of ice accretion is linearly proportional with LWC when other conditions are unchanged. Scallop formation is observed when the cylinder angle with the direction perpendicular to the flow is large enough. The dependence of scallop formation on the angle between the cylinder and flow, on LWC and on air velocity coincides with the observations of previous studies made during icing of aircraft wing tips. The importance of this result is emphasized by the fact that the same phenomena are observed at low velocities and on different geometry. Thus, scallop formation can be studied even in low-speed wind tunnels on an icing object with such simple geometry as a cylinder.

### **Acknowledgments**

This work was carried out within the framework of the NSERC/Hydro-Québec/UQAC Industrial Chair on Atmospheric Icing of Power Network Equipment (CIGELE) and the Canada Research Chair on Engineering of Power Network Atmospheric Icing (INGIVRE) at the University of Québec at Chicoutimi. The authors would like to thank the CIGELE partners (Hydro-Québec, Hydro One, Réseau Transport d'Électricité (RTE) and Électricité de France (EDF), Alcan Cable, K-Line Insulators, Tyco Electronics, CQRDA and FUQAC) whose financial support made this research possible. The valuable help provided by P. Camirand in designing and making devices for the experimental investigation is also acknowledged.

### **References**

- [1] Vargas, M., Giriunas, J.A., Ratvasky, T.P., Ice Accretion Formations on a NACA 0012 Swept Wing Tip in Natural Conditions, AIAA Paper 2002-0244, 2002.

- [2] Makkonen, L., Models of the growth of rime, glaze, icicles and wet snow on structures, *Phil Trans Royal Soc London A* 358 (2000) 2913-2939.
- [3] Lozowski, E.P., Makkonen, L., Fifty Years of Progress in Modelling the Accumulation of Atmospheric Ice on Power Network Equipment, *Proc of 11th Int Workshop on Atmospheric Icing of Structures*, Montreal, QC, Canada, 2005, pp. 55-62.
- [4] Vargas, M., Current Experimental Basis for Modeling Ice Accretions on Swept Wings, *AIAA Paper 2005-5188*, 2005.
- [5] AFGL, *Handbook of Geophysics and Space Environment*, Hanscom AFB, MA, 1985.
- [6] Jeck, R.K., Representative Values of Icing-Related Variables Aloft in Freezing Rain and Freezing Drizzle, *DOT/FAA/AR-TN95/119*, 1996.
- [7] Jeck, R.K., Icing Design Envelopes (14 CFR Parts 25 and 29, Appendix C) Converted to a Distance-Based Format, *DOT/FAA/AR-00/30*, 2002.
- [8] Karev, A.R., Farzaneh, M., Kollár, L.E., Vaslon, S., New Dynamic Aspects of Contemporaneous Concepts in Atmospheric Icing Modelling, *17th International Symposium on Ice*, St-Petersburg, Russia, 2004, pp. 413-418.
- [9] Kollár, L.E., Farzaneh, M., Spray Characteristics of Artificial Aerosol Clouds in a Low-Speed Icing Wind Tunnel, *Atomization and Sprays* 19 (4) (2009) 389-407.
- [10] Kollár, L.E., Farzaneh, M., Karev, A.R., Modeling Droplet Size Distribution Near a Nozzle Outlet in an Icing Wind Tunnel, *Atomization and Sprays* 16 (6) (2006) 673-686.
- [11] Lebatto, E.B., *Élaboration d'un modèle morphogénétique d'accrétion de glace en 3D sur un cylindre représentant un conducteur de ligne aérienne hors tension et étude comparative avec des résultats expérimentaux (Elaboration of a 3D morphogenetic ice accretion model on a cylinder representing a non-energized power network line conductor as compared to experimental results, in French)*, PhD thesis, University of Quebec at Chicoutimi, Chicoutimi, 2008.
- [12] Lozowski, E.P., Stallabrass, J.R., Hearty, P.F., The Icing of an Unheated, Nonrotating Cylinder. Part I: A Simulation Model, *Journal of Climate and Applied Meteorology* 22 (1983) 2053-2062.

- [13] Lozowski, E.P., Stallabrass, J.R., Hearty, P.F., The Icing of an Unheated, Nonrotating Cylinder. Part II: Icing Wind Tunnel Experiments, *Journal of Climate and Applied Meteorology* 22 (1983) 2063-2074.
- [14] Mohler Jr., S.R., Bidwell, C.S., Comparison of Two-dimensional and Three-dimensional Droplet Trajectory Calculations in the Vicinity of Finite Wings, NASA TM-105617, AIAA-92-0645, 1992.

## Figure Captions

Fig. 1: Angles of inclination, (a) angle,  $\alpha$ , varied around streamwise axis in vertical plane, (b) angle,  $\beta$ , varied around vertical axis in horizontal plane, (c) angle,  $\gamma$ , varied around lateral axis in vertical plane

Fig. 2: Schema of the wind tunnel from the spray bar section to the test section with a cylinder in horizontal position perpendicularly to the flow (not to scale)

Fig. 3: Horizontal spray bar with three nozzles which inject droplets horizontally

Fig. 4: Nozzle on the ceiling of test section for injecting droplets vertically

Fig. 5: Profiles of ice accretions for various values of angle,  $\alpha$ , around streamwise axis under CI conditions with increased LWC [8]

Fig. 6: Profiles of ice accretions for various values of angle,  $\alpha$ , around streamwise axis under ZR conditions [8]

Fig. 7: Profile, top, front and bottom views of ice accretions for  $\alpha = 4^\circ$ , (a) CI conditions, (b) CI conditions with increased LWC [8], (c) ZR conditions [8]

Fig. 8: The ratio of ice accretion mass per unit length on the inclined cylinder to that on the horizontal one versus the cylinder angle  $\alpha$ , (a) CI conditions with normal (CI\_1) and with increased (CI\_3.2) LWC,  $m_{CI,\alpha_0}$  – ice mass obtained under CI conditions with increased LWC for  $\alpha = 0^\circ$ , (b) ZR conditions,  $m_{ZR,\alpha_0}$  – ice mass obtained under ZR conditions for  $\alpha = 0^\circ$ ; “up” and “low” in legend refer to ice samples from the upper and lower parts of the cylinder, respectively; \* – present study, \*\* – [8]

Fig. 9: The effects of air temperature and air velocity on the ice accretion mass per unit length under CI conditions with increased LWC for  $\alpha = 0^\circ$ ;  $m_{CI,\alpha_0}$  – ice mass obtained under CI conditions with increased LWC for  $\alpha = 0^\circ$ ,  $T_{a,SB} = -10^\circ\text{C}$  ( $T_{a,TS} = -8.7^\circ\text{C}$ ),  $V_a = 20\text{ m/s}$

Fig. 10: Time evolution of the shape of ice deposits accreted for angles of  $\alpha = 4^\circ$  (left) and  $\alpha = 28^\circ$  (right) under CI conditions with increased LWC [8]

Fig. 11: Profiles of ice accretions for various values of angle,  $\beta$ , around vertical axis under CI conditions with increased LWC

Fig. 12: Top views of ice accretions for various values of angle,  $\beta$ , around vertical axis, (a) CI conditions, (b) CI conditions with increased LWC, (c) ZR conditions

Fig. 13: Relative ice mass per unit length versus the cylinder angle,  $\beta$ , (a) CI conditions with normal (CI\_1) and with increased (CI\_3.2) LWC,  $m_{Clup,\beta_0}$  – ice mass obtained under CI conditions with increased LWC upstream of cylinder midpoint for  $\beta = 0^\circ$ , (b) ZR conditions,  $m_{ZR,\beta_0}$  – ice mass obtained under ZR conditions for  $\beta = 0^\circ$ ; “up” and “down” in legend refer to ice samples from upstream and downstream of cylinder midpoint, respectively

Fig. 14: Side views of ice accretions for various values of the angle,  $\gamma$ , around lateral axis under CI conditions with increased LWC [8]

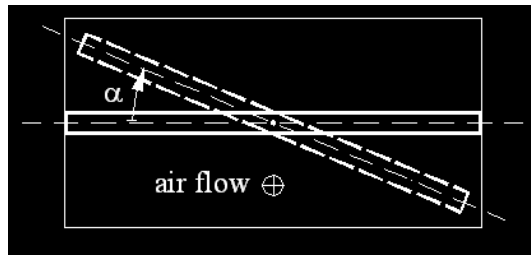
Fig. 15: Profiles (left) and top or side views (right) of ice accretions for various values of the angle,  $\gamma$  around lateral axis under ZR conditions [8]

Fig. 16: Relative ice mass per unit length versus the cylinder angle,  $\gamma$ , obtained in [8];  $m_{ZRup,\gamma_0}$  – ice mass obtained under ZR conditions upstream of cylinder midpoint for  $\gamma = 90^\circ$ ; “up” and “down” in legend refer to ice samples from upstream and downstream of cylinder midpoint, respectively

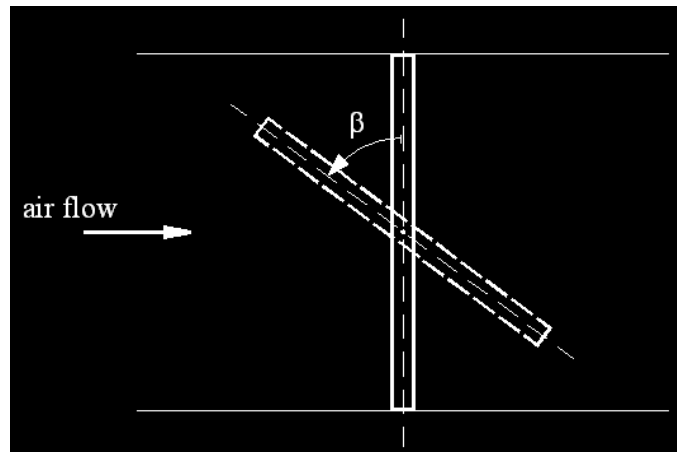
## Tables

$T_{a,SB}$ ( $^{\circ}\text{C}$ )	$\Delta T_{a,SB}$ ( $^{\circ}\text{C}$ )	$T_{a,TS}$ ( $^{\circ}\text{C}$ )	$\Delta T_{a,TS}$ ( $^{\circ}\text{C}$ )
-5	$\pm 1.0$	-4.5	$\pm 1.3$
-10	$\pm 0.8$	-8.7	$\pm 1.0$
-15	$\pm 0.8$	-13.1	$\pm 1.0$
-20	$\pm 0.2$	-17.5	$\pm 0.4$

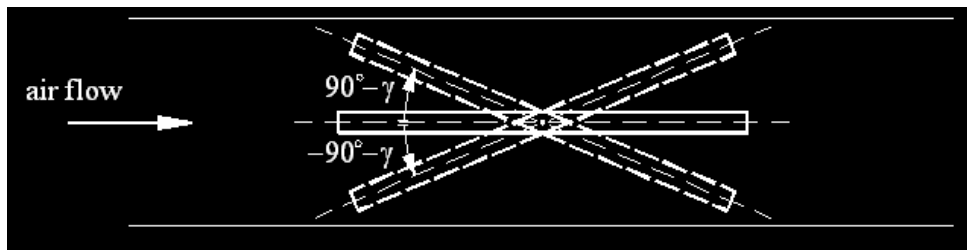
Table 1: Air temperature data in the tunnel and their fluctuations;  $T_{a,SB}$ ,  $T_{a,TS}$  – air temperatures in tunnel section preceding spray bar and in test section, respectively;  $\Delta T_{a,SB}$ ,  $\Delta T_{a,TS}$  – fluctuation in air temperature in tunnel section preceding spray bar and in test section, respectively



(a)



(b)



(c)

Fig. 1: Angles of inclination, (a) angle,  $\alpha$ , varied around streamwise axis in vertical plane, (b) angle,  $\beta$ , varied around vertical axis in horizontal plane, (c) angle,  $\gamma$ , varied around lateral axis in vertical plane

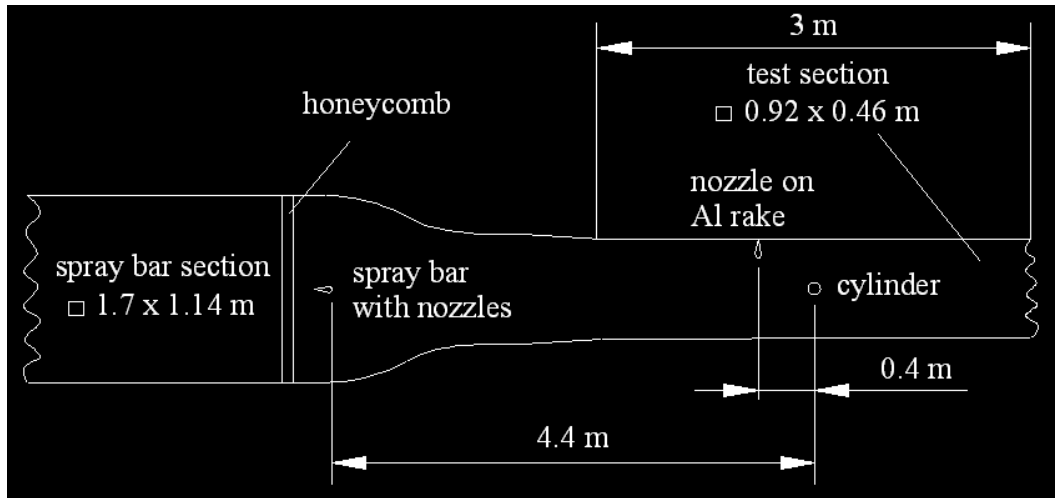


Fig. 2: Schema of the wind tunnel from the spray bar section to the test section with a cylinder in horizontal position perpendicularly to the flow (not to scale)



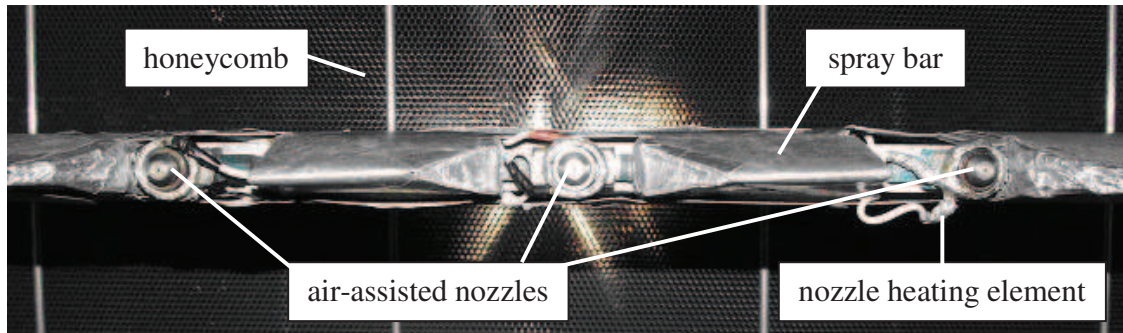


Fig. 3: Horizontal spray bar with three nozzles which inject droplets horizontally

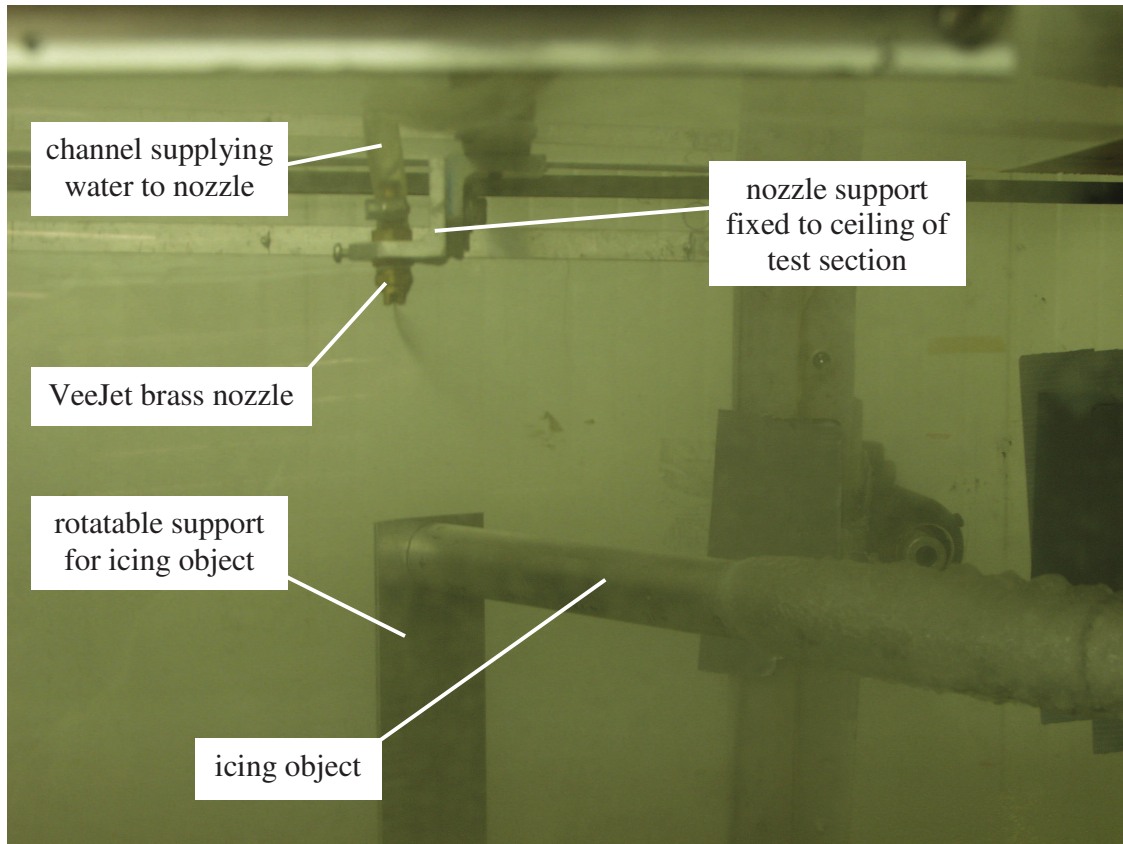


Fig. 4: Nozzle on the ceiling of test section for injecting droplets vertically

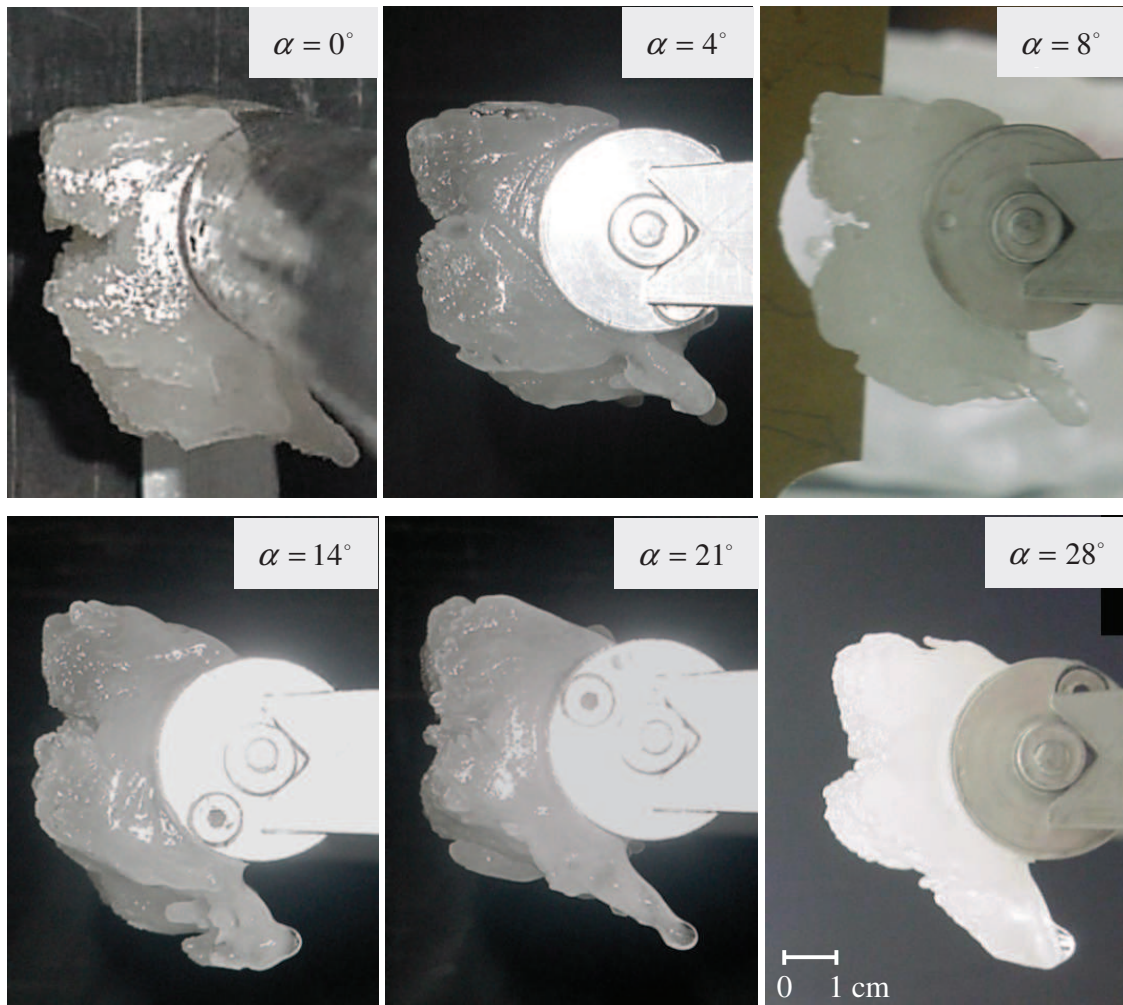


Fig. 5: Profiles of ice accretions for various values of angle,  $\alpha$ , around streamwise axis under CI conditions with increased LWC [8]

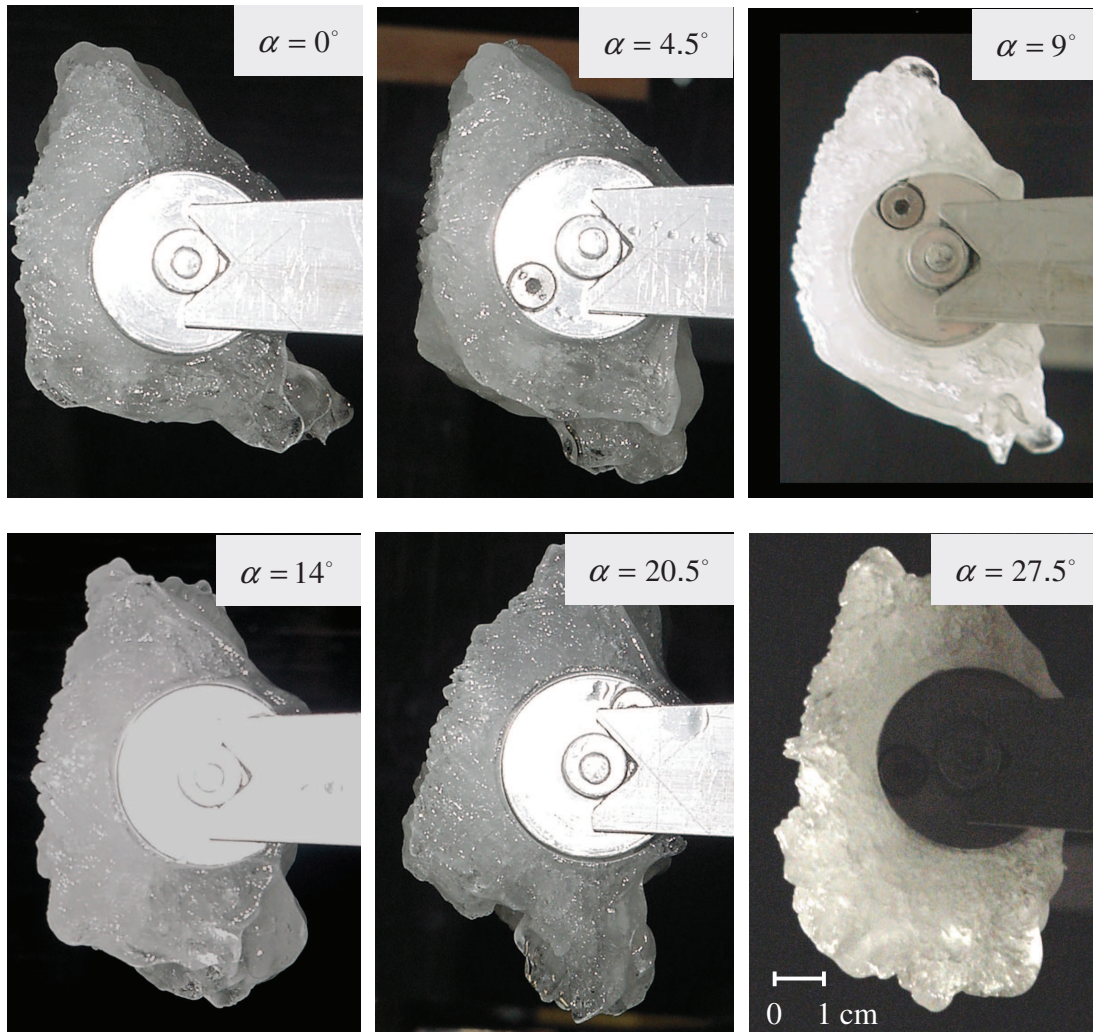


Fig. 6: Profiles of ice accretions for various values of angle,  $\alpha$ , around streamwise axis under ZR conditions [8]



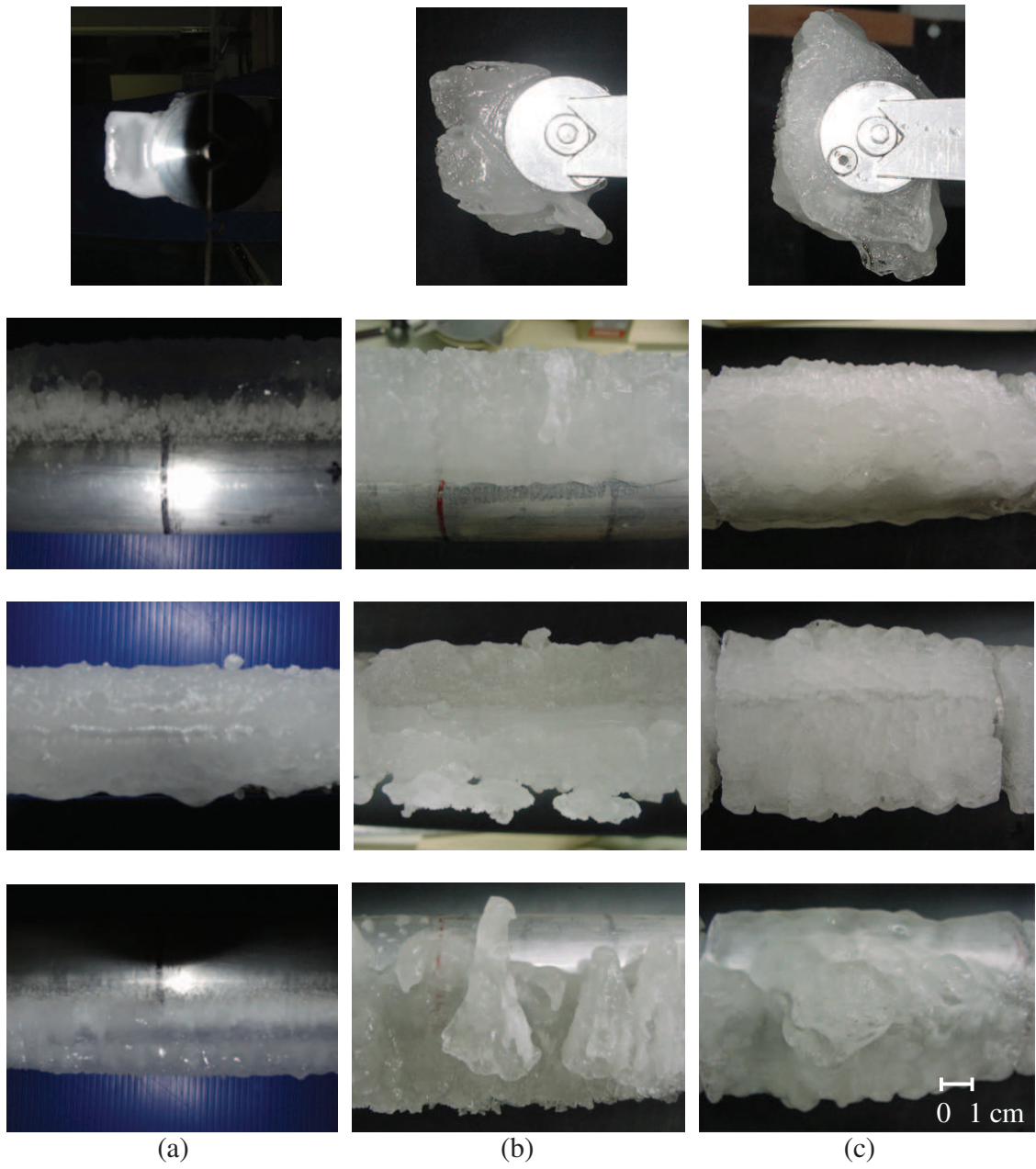
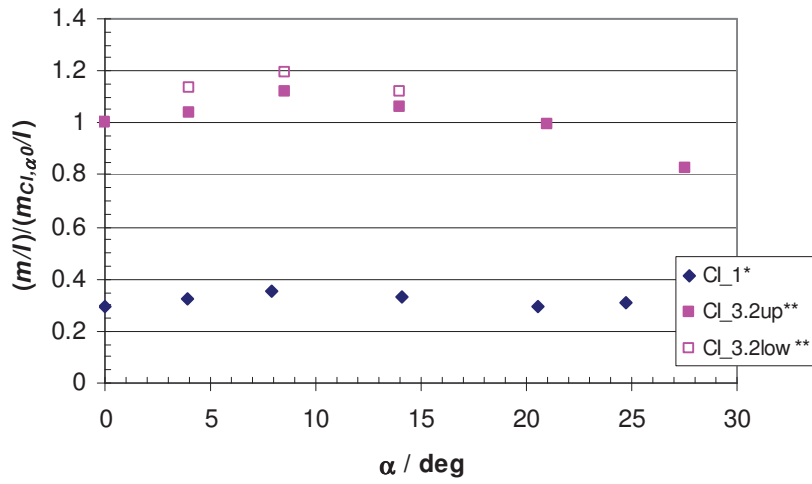
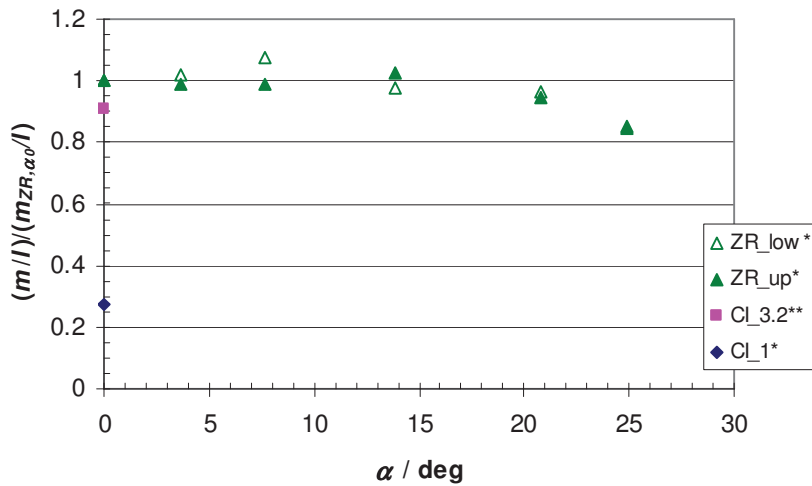


Fig. 7: Profile, top, front and bottom views of ice accretions for  $\alpha = 4^\circ$ , (a) CI conditions, (b) CI conditions with increased LWC [8], (c) ZR conditions [8]



(a)



(b)

Fig. 8: The ratio of ice accretion mass per unit length on the inclined cylinder to that on the horizontal one versus the cylinder angle  $\alpha$ , (a) CI conditions with normal (CI\_1) and with increased (CI\_3.2) LWC,  $m_{CI,\alpha_0}$  – ice mass obtained under CI conditions with increased LWC for  $\alpha = 0^\circ$ , (b) ZR conditions,  $m_{ZR,\alpha_0}$  – ice mass obtained under ZR conditions for  $\alpha = 0^\circ$ ; “up” and “low” in legend refer to ice samples from the upper and lower parts of the cylinder, respectively; \* – present study, \*\* – [8]

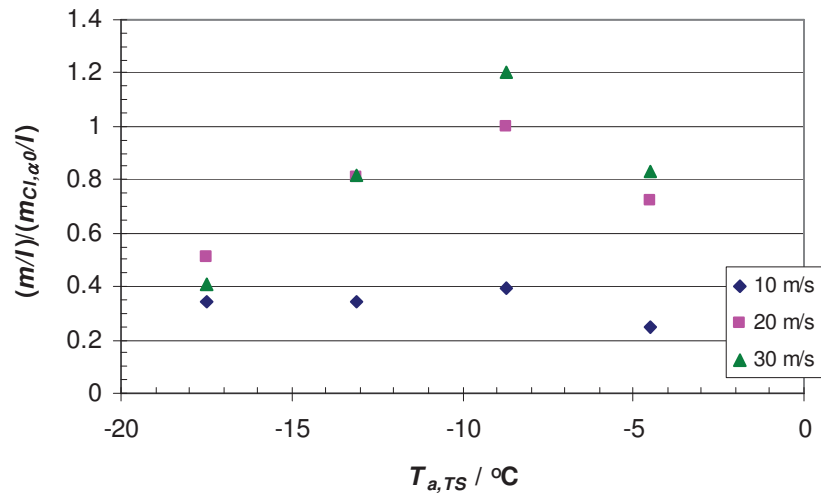


Fig. 9: The effects of air temperature and air velocity on the ice accretion mass per unit length under CI conditions with increased LWC for  $\alpha = 0^\circ$ ;  $m_{CI, \alpha_0}$  – ice mass obtained under CI conditions with increased LWC for  $\alpha = 0^\circ$ ,  $T_{a, SB} = -10^\circ\text{C}$  ( $T_{a, TS} = -8.7^\circ\text{C}$ ),  $V_a = 20\text{ m/s}$

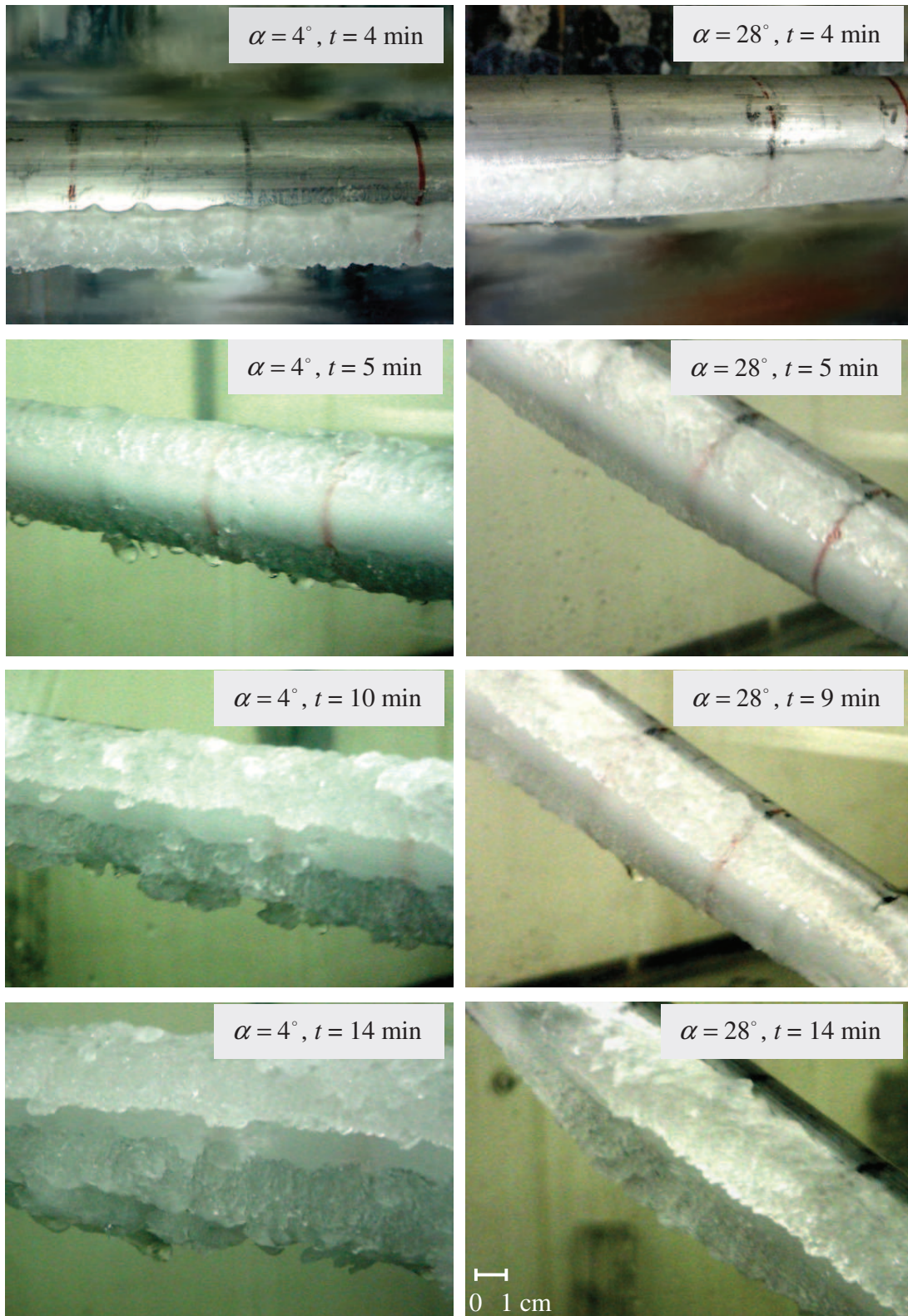


Fig. 10: Time evolution of the shape of ice deposits accreted for angles of  $\alpha = 4^\circ$  (left) and  $\alpha = 28^\circ$  (right) under CI conditions with increased LWC [8]



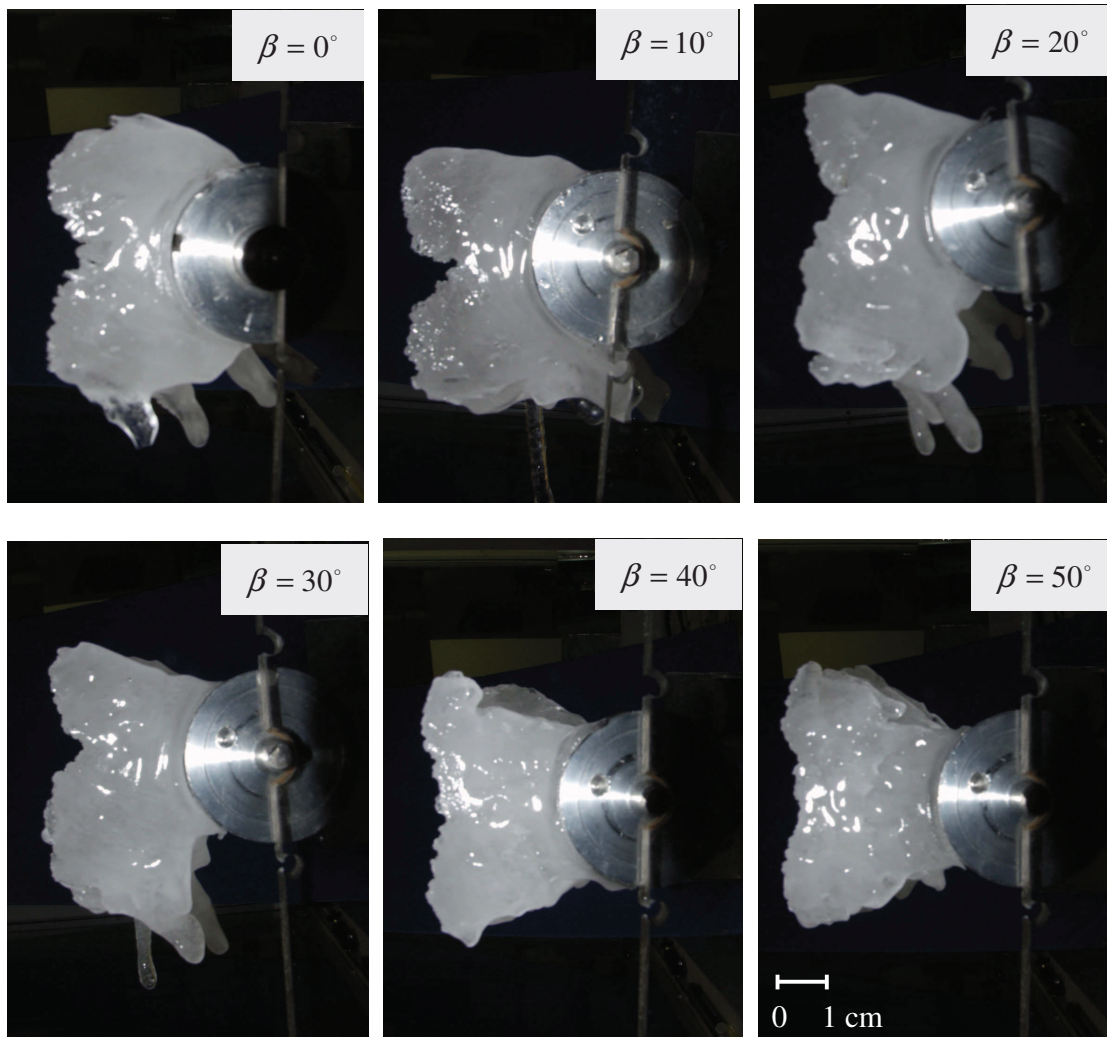


Fig. 11: Profiles of ice accretions for various values of angle,  $\beta$ , around vertical axis under CI conditions with increased LWC

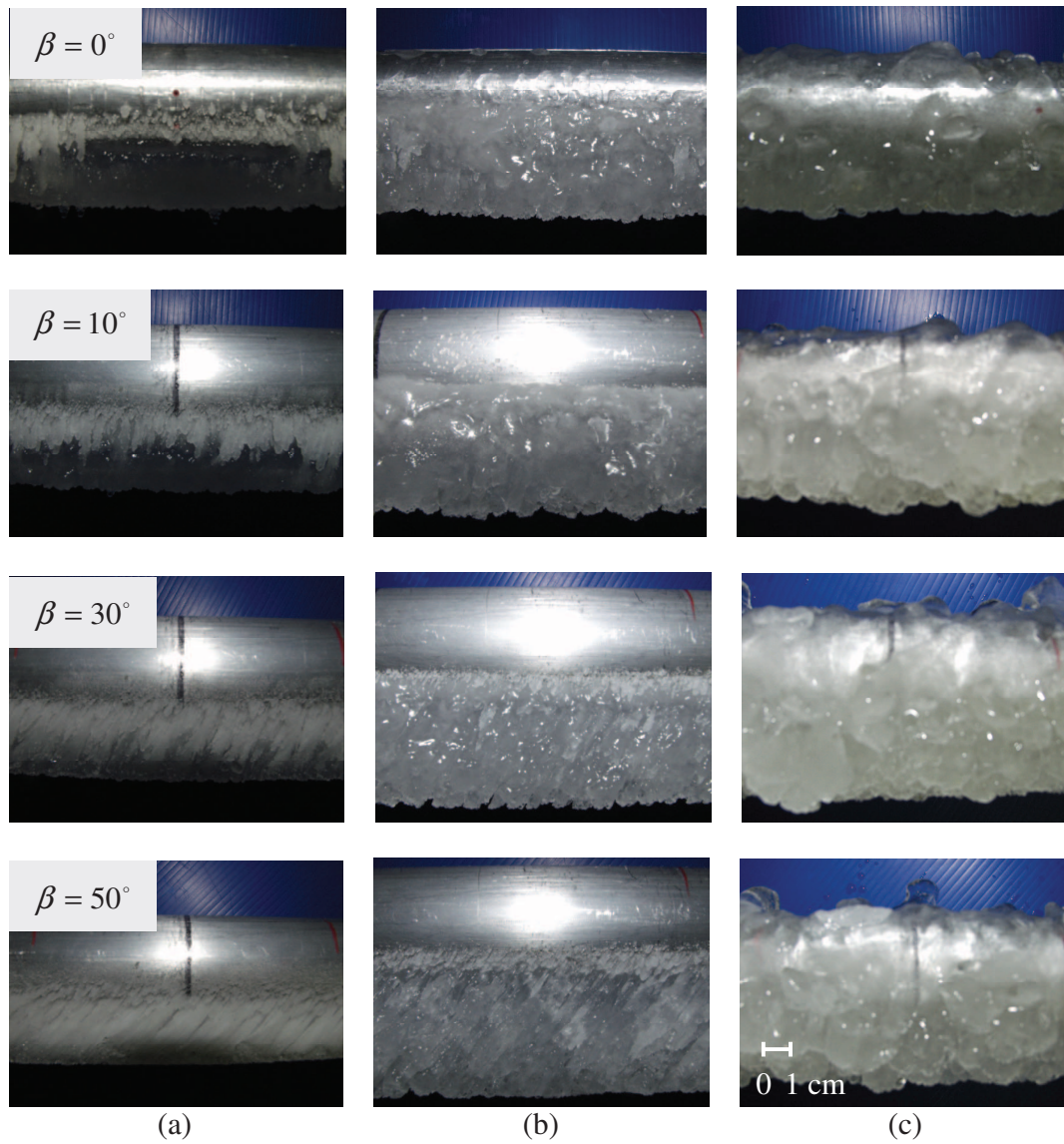
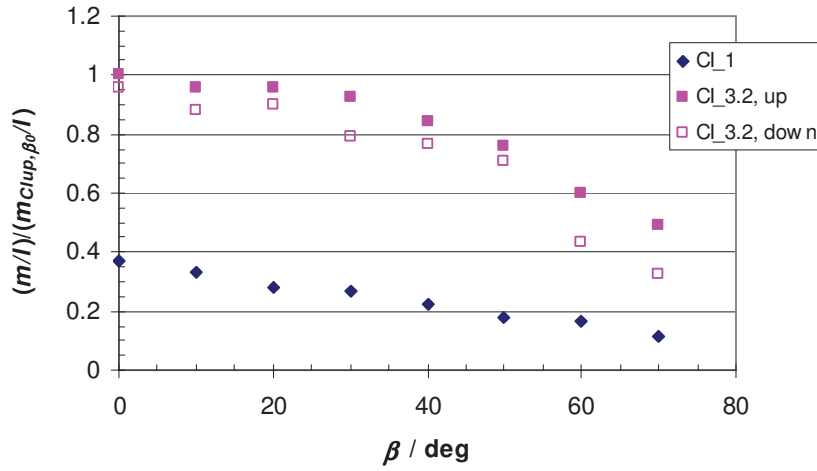
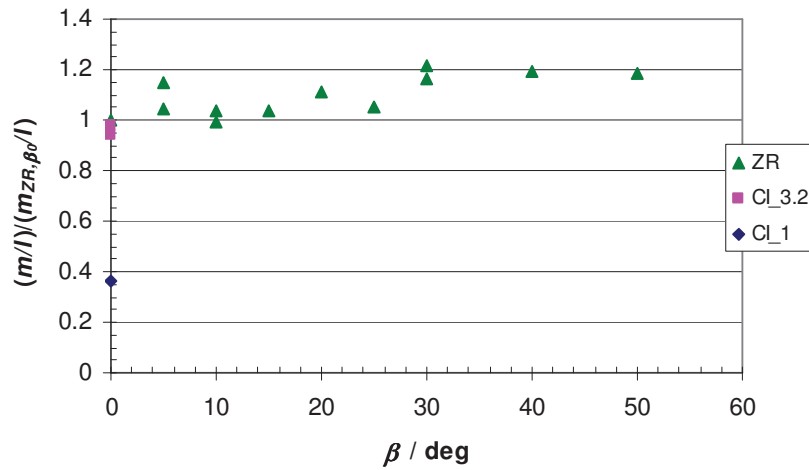


Fig. 12: Top views of ice accretions for various values of angle,  $\beta$ , around vertical axis, (a) CI conditions, (b) CI conditions with increased LWC, (c) ZR conditions



(a)



(b)

Fig. 13: Relative ice mass per unit length versus the cylinder angle,  $\beta$ , (a) CI conditions with normal (CI\_1) and with increased (CI\_3.2) LWC,  $m_{CI_{up},\beta_0}$  – ice mass obtained under CI conditions with increased LWC upstream of cylinder midpoint for  $\beta = 0^\circ$ , (b) ZR conditions,  $m_{ZR,\beta_0}$  – ice mass obtained under ZR conditions for  $\beta = 0^\circ$ ; “up” and “down” in legend refer to ice samples from upstream and downstream of cylinder midpoint, respectively

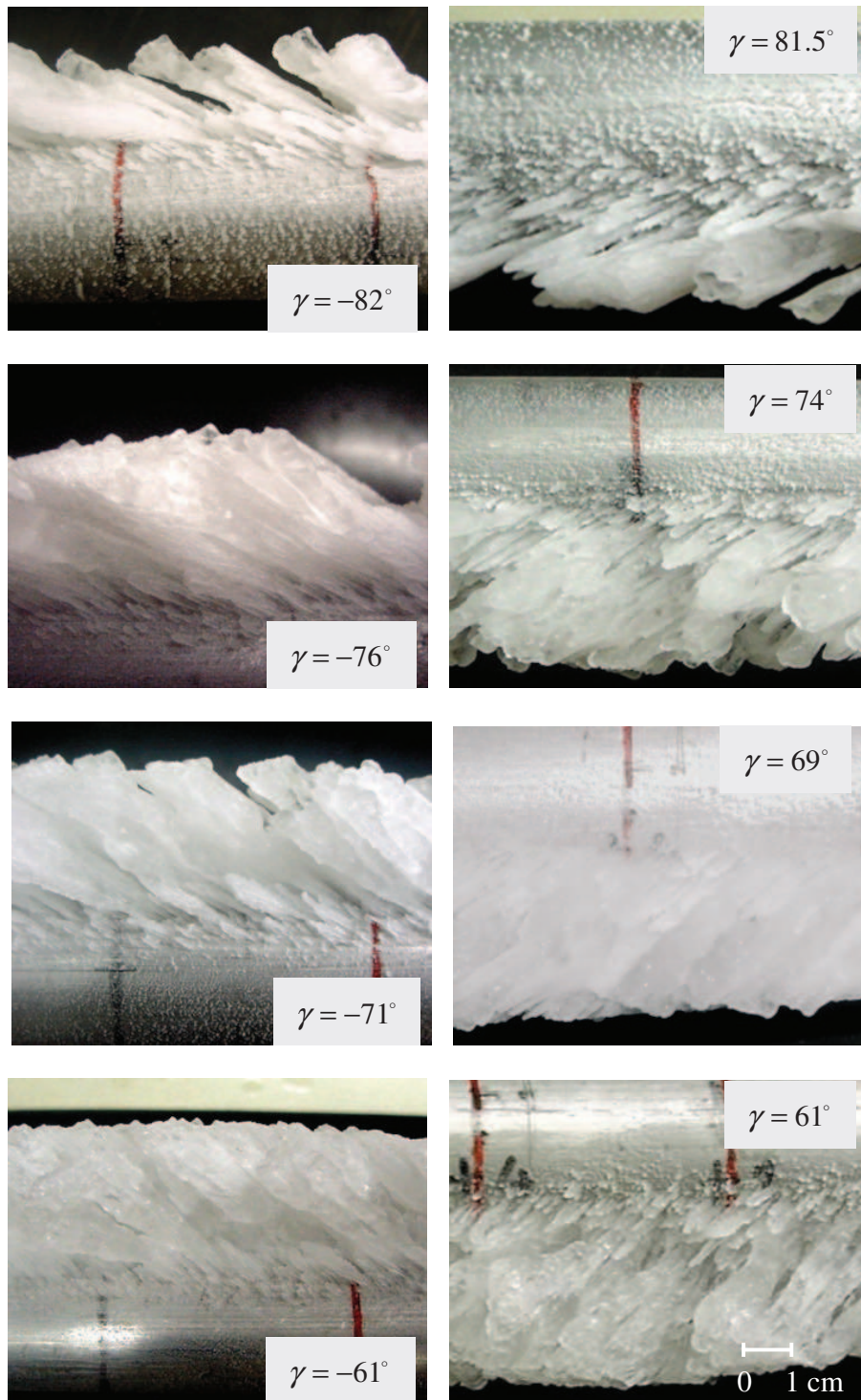


Fig. 14: Side views of ice accretions for various values of the angle,  $\gamma$ , around lateral axis under CI conditions with increased LWC [8]



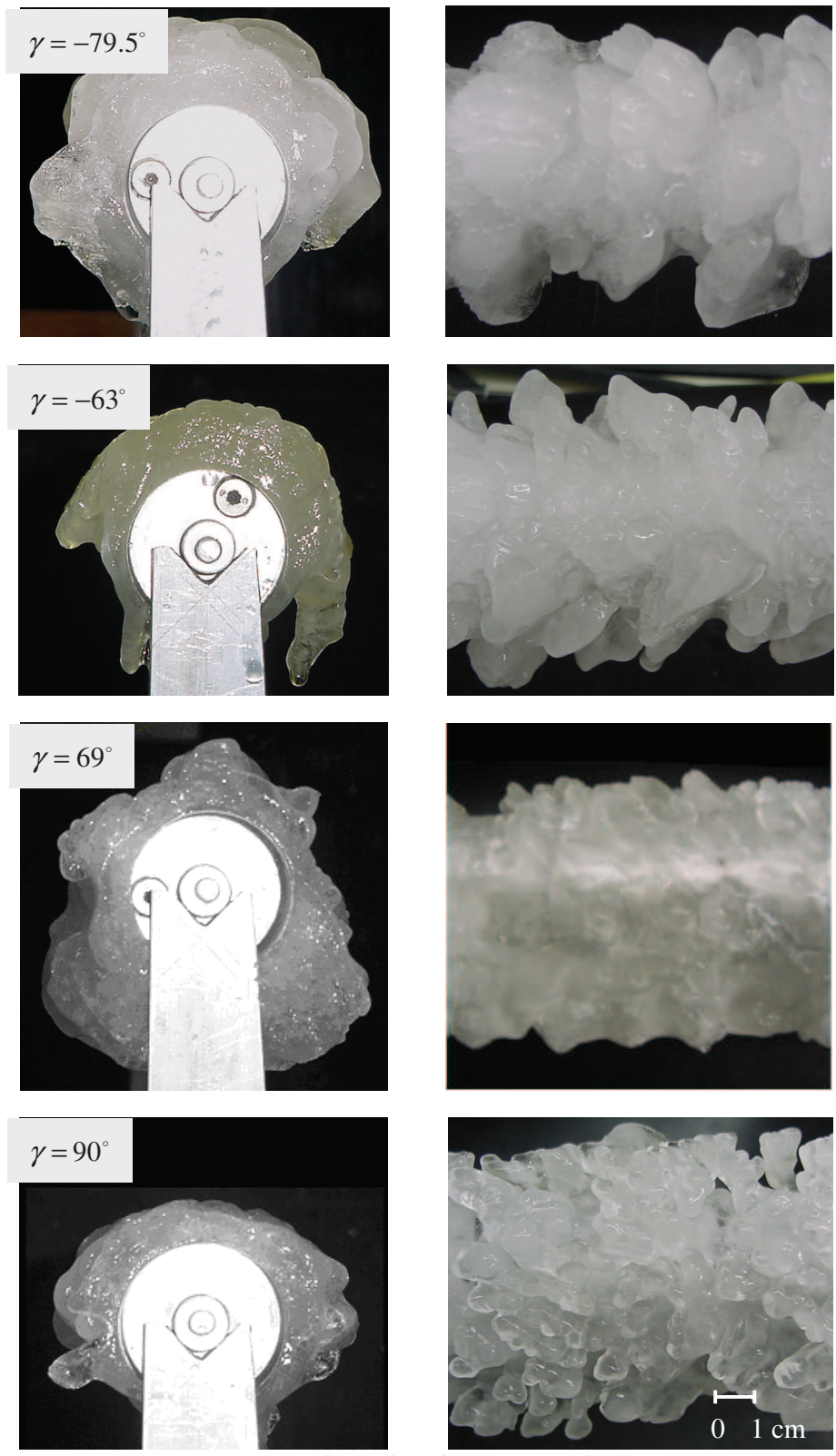


Fig. 15: Profiles (left) and top ( $-79.5^\circ$ ,  $-63^\circ$ ,  $90^\circ$ ) or side ( $69^\circ$ ) views (right) of ice accretions for various values of the angle,  $\gamma$ , around lateral axis under ZR conditions [8]

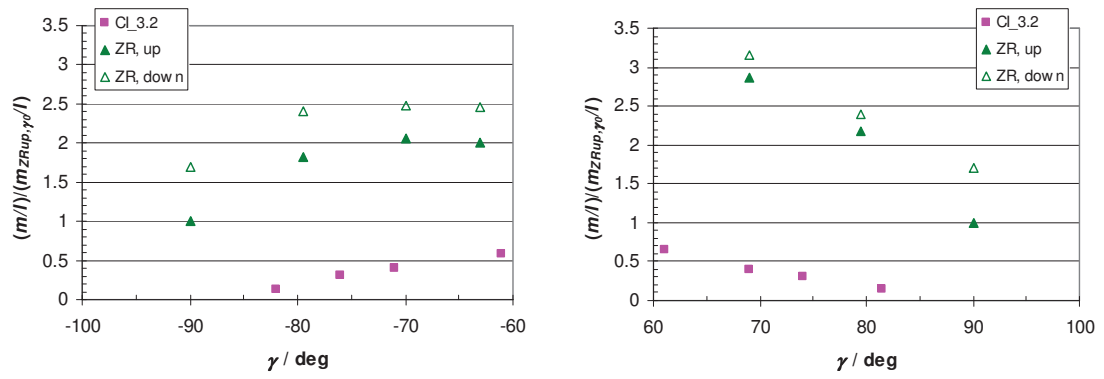


Fig. 16: Relative ice mass per unit length versus the cylinder angle,  $\gamma$ , obtained in [8];  $m_{ZRup,\gamma_0}$  – ice mass obtained under ZR conditions upstream of cylinder midpoint for  $\gamma = 90^\circ$ ; “up” and “down” in legend refer to ice samples from upstream and downstream of cylinder midpoint, respectively